# Nanocrystal-based thermoelectric SnTe-$NaSbSe_2$ alloys with strengthened band convergence and reduced thermal conductivity

Bingfei Nan [a, b], Cheng Chang [c], Nilotpal Kapuria [d, e, *], Xu Han [f], Mengyao Li [g], Kevin M. Ryan [d], Jordi Arbiol [f, h], Andreu Cabot [a, h, *]

[a] Catalonia Institute for Energy Research—IREC, Sant Adrià de Besòs, Barcelona 08930, Spain

[b] Universitat de Barcelona, Martí i Franquès 1, 08028, Barcelona, Spain

[c] School of Materials Science and Engineering, Beihang University, Beijing 100191, China.

[d] Department of Chemical Sciences and Bernal Institute, University of Limerick, V94T9PX Limerick, Ireland

[e] Indiana University, Department of Chemistry 800 E. Kirkwood, CHEM Bloomington, IN 47405-7102

[f] Catalan Institute of Nanoscience and Nanotechnology (ICN2), Campus UAB, Bellaterra, Barcelona 08193, Catalonia, Spain

[g] Key Laboratory of Material Physics of Ministry of Education, School of Physics and Microelectronics, Zhengzhou University, Zhengzhou 450001, China

[h] ICREA, Pg. Lluís Companys 23, 08010 Barcelona, Catalonia, Spain

Email: nkapuria@iu.edu (N. Kapuria), acabot@irec.cat (A. Cabot).

## ABSTRACT

Ternary I-V-$VI_2$ colloidal $NaSbSe_2$ nanocrystals are herein used to improve the performance of lead-free SnTe thermoelectric materials. We showcase a versatile bottom-up engineering approach to produce SnTe-$NaSbSe_2$ alloys from the rapid hot press of colloidal nanocrystal building blocks. The incorporation of $NaSbSe_2$ nanocrystals significantly enhances the Seebeck coefficient of SnTe. Besides, Sn vacancies, substitution point defects, dislocations, and strains generated by the $NaSbSe_2$ nanoparticles incorporation result in a dramatic reduction of the lattice thermal conductivity below the amorphous limit of pure SnTe, down to 0.38 W $m^{-1}K^{-1}$. As a consequence, power factors enhance up to 1.77 mW $m^{-1}K^{-2}$, which is ~193% higher than

that of the pristine SnTe, and thermoelectric figures of merit up to 1.15 at 823 K for $(SnTe)_{0.85}(NaSbSe_2)_{0.15}$ are achieved.

**Keywords**: Thermoelectric; Nanocrystals; SnTe; $NaSbSe_2$; alloy; Sn vacancies

## 1. Introduction

Thermoelectric (TE) technology enables direct conversion of heat into electricity and vice versa. Thus, TE devices can be used for waste heat recovery and solid-state cooling [1-5]. The performance of TE materials is quantified by a figure of merit, $ZT = \frac{\sigma S^2 T}{\kappa_{ele}+\kappa_{lat}}$, where σ, S, T, $\kappa_{ele}$, and $\kappa_{lat}$ are the electrical conductivity, Seebeck coefficient, absolute temperature, electronic thermal conductivity, and lattice thermal conductivity, respectively. The sum of the contributions from $\kappa_{ele}$ and $\kappa_{lat}$ is the total thermal conductivity $\kappa_{tot}$. Given the strong coupling among S, σ, and $\kappa_e$, improving these parameters individually to enhance zT effectively is a huge challenge. Being $\kappa_{lat}$ a less dependent parameter, several strategies to reduce $\kappa_{lat}$ have been put into practice [6, 7].

PbTe is one of the main TE materials for medium-temperature applications. However, its industrialization is limited by Pb toxicity. SnTe is a Pb-free analogy to PbTe that is also characterized by a *p*-type conductivity, but a moderate Seebeck coefficient generally limits its TE performance. This limited Seebeck coefficient is related to two main parameters. On the one hand, SnTe is usually characterized by too high intrinsic hole concentration associated with a high density of Sn vacancies ($10^{20}$–$10^{21}$ $cm^{-3}$) that results in moderate Seebeck coefficients and high electronic thermal conductivity [8]. On the other hand, within SnTe, the relatively large energy gap between the L and Σ bands, $\Delta E_{L-\Sigma} \sim 0.3$ eV in SnTe limits the contribution of the high valley degenerate Σ-band, which again results in poorer Seebeck coefficients compared to PbTe [9]. To overcome these limitations, several cationic dopants have been introduced into SnTe, including Ag [10], Na[11], Zn [12], In [13], Sb [14], Bi [15], Mg [16], Ga [17] and V [18]. While atomic doping has shown some success in reducing the overall thermal conductivity, the enhancement of the Seebeck coefficient has been moderate.

An alternative approach to improve the TE performance of SnTe is combining this material

with a second compound into an alloy or a composite. The introduction of additional phases generally creates a variety of defects that enhance phonon scattering, but its effect on the power factor is usually limited. A particularly interesting case is the combination of tin chalcogenides with I−V−$VI_2$ compounds (I= Ag, Li, Na; V=Sb, Bi; and VI=Se, Te). These alloys/composites, which were first explored in the 1960s [19], demonstrate notable performance when using I−V−$VI_2$ compounds such as $AgSbSe_2$ [20], $AgSbTe_2$ [21, 22], $AgBiSe_2$ [23], $AgBiTe_2$ [24, 25], $NaSbTe_2$ and $NaBiTe_2$ [8, 26, 27]. In these rock-salt-based I−V−$VI_2$ compounds, there is strong hybridization and repulsion between the lone $ns^2$ pair electrons of group V cations and the p-orbitals of group $VI_2$ anions, resulting in strong phonon-phonon interactions [26, 28]. For instance, Slade et al. showed that alloying SnTe with $NaSbTe_2$ significantly increases the concentration of Sn vacancies [8]. Contrary to the usual expectation that an increase in vacancies and thus hole concentration would decrease the Seebeck coefficient, their research found the opposite effect. The higher Sn vacancy concentration results in a convergence of the valence band and a reduction in the bandgap increasing the Seebeck coefficient. Benefiting from the favorable effects of band convergence, vacancy-enhanced hole concentration, and lattice softening, a high ZT value of 1.2 at 800–900 K was achieved.

As an alternative to $NaSbTe_2$, the Te-free $NaSbSe_2$ shows promising potential in areas such as solar cells [29, 30], and like other similar compounds such as $NaSbTe_2$ and $NaBiTe_2$ is known to exist in a cation-disordered NaCl-like cubic structure. Inspired by the valence band convergence, band gap narrowing, and low sound velocity of SnTe/$NaSbTe_2$ alloys, it is of interest to examine whether the introduction of other rock-salt compounds can optimize the thermal and electrical properties of SnTe [31-34].

Our previous research has demonstrated that controlling the chemical composition of TE materials at the nanoscale through multi-component alloy engineering can effectively improve the TE properties of the materials [31, 35-37]. This work for the first time demonstrates a feasible approach to engineering a SnTe alloy with I-V-$VI_2$ compounds, mainly using colloidal $NaSbSe_2$ nanocrystals (NCs) as building blocks. We further show the formed alloys to be characterized by exceptional transport properties and TE performance.

## 2. Results and discussion

Gram-scale batches of SnTe nanoparticles (NPs) were produced using a high-yield and scalable thermal decomposition approach at 280 °C. As described in the experimental methods (Supporting Information, SI), to prepare SnTe NPs, $Sn^{2+}$ ion salts were first coordinated with oleylamine (OAm) to form Sn-OAm complexes and afterward combined with tri-n-octylphosphine telluride (TOPTe). The obtained precursor was quickly heated to 280 °C and kept in an Ar atmosphere for 1 h to obtain SnTe NPs with good crystallinity. The synthesis method used was highly scalable, allowing the facile production of ~6.2 g of high-quality SnTe NCs per batch (Figure 1a). Figure 1b shows a high-resolution transmission electron microscopy (HRTEM) micrograph of the produced SnTe NCs. The fast Fourier transform (FFT) of the HRTEM image reveals that this nanostructure has a crystal phase that can be assigned to the cubic rock-salt SnTe phase (space group=$Fm\bar{3}m$) with a=b=c=6.2900 Å. Most of the obtained SnTe NCs display irregular but faceted morphologies and a size of about ~100 nm, as shown by high-angle annular dark field scanning transmission electron microscopy (HAADF-STEM, Figures 1c and S1). Electron energy loss spectroscopy (EELS) chemical composition maps obtained from the red squared regions in the HAADF-STEM micrograph show a homogeneous distribution of Sn and Te. Powder X-ray diffraction (XRD) patterns revealed all diffraction peaks to match well with the cubic rock-salt crystal structure of SnTe (space group $Fm\bar{3}m$, PDF 00-008-0487, Figure 1h), which is also consistent with the results derived from HRTEM analyses.

$NaSbSe_2$ NCs were produced using a colloidal hot injection route [34]. Briefly, a sodium oleate solution was combined with metal Sb acetate in a mixed solvent system of OAm and 1-octadecene (ODE), and degassed at 105 °C for 1h to remove low-boiling point impurities. Subsequently, a thiol-Se complex was injected at 240 °C under an Ar atmosphere. Detailed procedures can be found in the experimental section (SI). $NaSbSe_2$ NCs show a spherical shape with an average size of ~44 ± 12 nm (Figure 1d, e). Figure 1f shows an HRTEM image of the produced $NaSbSe_2$ NCs. STEM-EDS line profiles show the presence of Na, Sb, and Se in the NCs (Figure 1g), and Na:Sb:Se stoichiometry of 1:1:2 is confirmed by SEM-EDS analysis (Figure S2). XRD patterns in Figure 1h exhibit the $NaSbSe_2$ NCs to have the expected cubic rock-salt crystal structure (space group $Fm\bar{3}m$, PDF 004-005-7023).

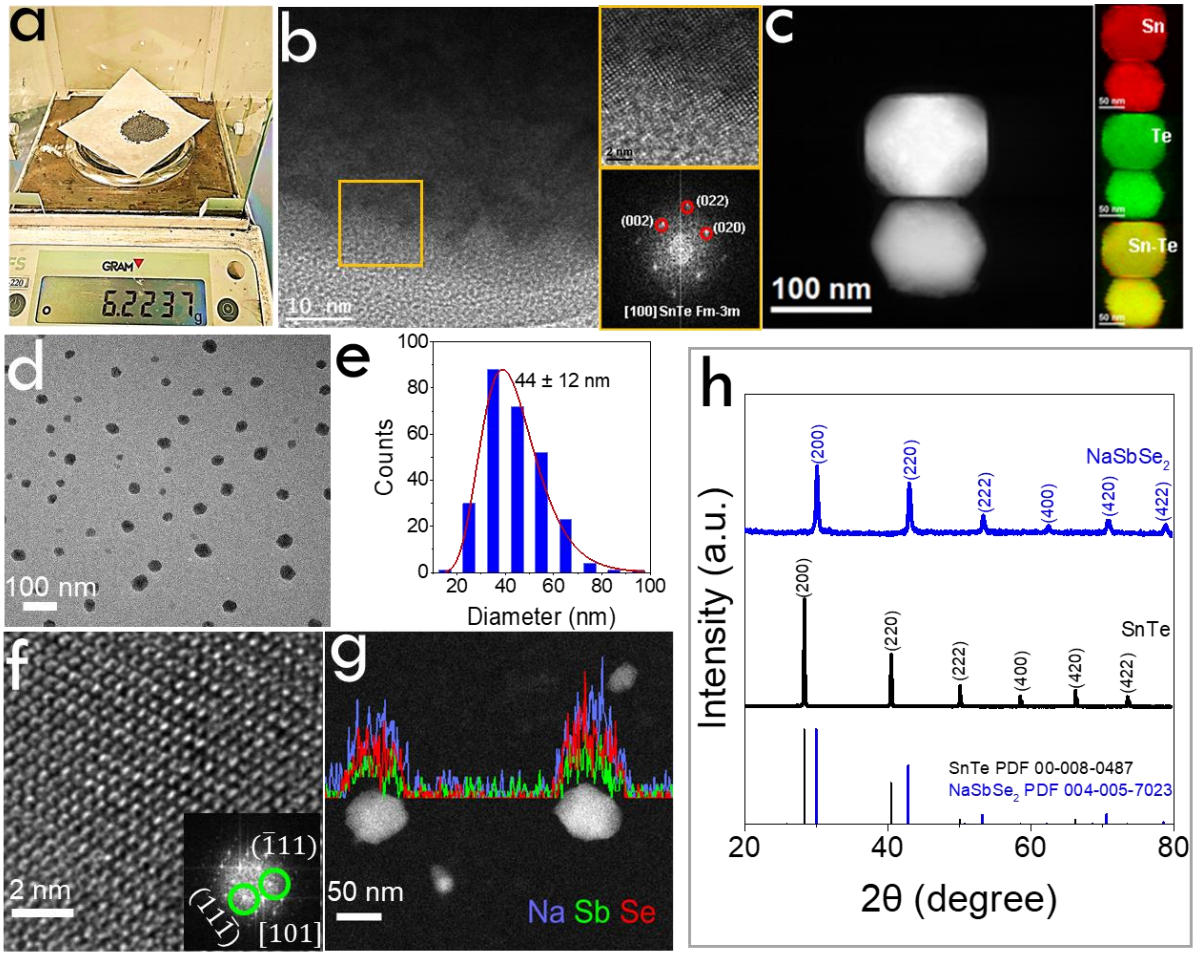


**Figure 1**. (a) Photograph of the amount of dried SnTe powders obtained in a single batch. (b) HRTEM micrograph, power spectrum, and detail of the orange squared region. From the crystalline domain, the SnTe lattice fringe distances were measured to be 0.318 nm, 0.223 nm, and 0.314 nm, at 45.06º and 90.40º which could be interpreted as the cubic SnTe phase, visualized along its [100] zone axis. (c) EELS chemical composition maps obtained from the area of the STEM micrograph. Individual Sn $M_{4,5}$-edges at 485 eV (red), Te $M_{4,5}$-edges at 572 (green), and Sn-Te. (d) TEM image of the $NaSbSe_2$ NCs. (e) Size distribution of the $NaSbSe_2$ NCs. (f) HRTEM image of a of $NaSbSe_2$ NCs, The inset shows the fast Fourier transform (FFT) of the corresponding HRTEM image. (g) The blue, green, and red lines in the representative STEM-EDS line scan profiles correspond to signals from Na, Sb and Se atoms, respectively. (h) Powder X-ray diffraction patterns (XRD) of the SnTe and $NaSbSe_2$ phases.

$(SnTe)_{1-x}(NaSbSe_2)_x$ materials were produced by mixing proper molar ratios (x=0, 0.05, 0.10, 0.15 and 0.20) of the colloidal SnTe and $NaSbSe_2$ NCs in hexane. The solvent was afterward removed by evaporation. SEM micrographs of the dried powders show a homogeneous mixture of the two phases (Figure 2a and Figure S3). After the solvent evaporation process, the obtained $(SnTe)_{1-x}(NaSbSe_2)_x$ powders were annealed at high temperatures to remove organic residues. The annealed particles almost maintain their uniformly dispersed geometries and single SnTe crystalline phase (Figure 2b, Figure S4 and S5. Subsequently, the powders were hot-pressed into round-like pellet alloys (Figure 2d). The fresh SEM fracture surface of a pellet shows that the consolidated particles have no obvious grain growth after hot pressing (Figure 2c and Figure S6). Besides, EDS composition maps prove that the content of various elements is consistent with the nominal composition (Table S1). XRD analysis was used to examine whether the annealed mixture of SnTe and $NaSbSe_2$ forms an alloy after the sintering process. The XRD patterns of $(SnTe)_{1-x}(NaSbSe_2)_x$ pellets are shown in Figure 2e. All the XRD patterns can be indexed with the NaCl-structure of SnTe (space group $Fm\bar{3}m$), with no diffraction peaks of $NaSbSe_2$ being discerned even in the x=0.15 sample. Only the enlarged XRD pattern of the sintered $(SnTe)_{0.8}(NaSbSe_2)_{0.2}$ pellet shows minor secondary phase peaks that could be assigned to Te- or Sb-based phases (Figure S7). As observed in the enlarged XRD view of the $2\theta$ between 28° and 29°, the (200) diffraction peaks of $(SnTe)_{1-x}(NaSbSe_2)_x$ samples shift to a higher angle compared to bare SnTe, indicating that the lattice parameter gradually shrinks with the incorporation of an increasing $NaSbSe_2$ content. This lattice shrinkage can be attributed to the incorporation of Na, Sb, and Se into the SnTe lattice taking into account that the ionic radius of $Na^+$ (0.97 Å) and $Sb^{3+}$ (~0.76 Å) are smaller than that of $Sn^{2+}$ (1.18 Å) [38, 39], and the ionic radius of $Se^{2-}$ (~1.84 Å) is smaller than that of $Te^{2-}$ (~2.07 Å) [40]. SnTe and $NaSbSe_2$ have similar cubic structures, and their lattice constants are 6.29 and 5.97 Å, respectively. As shown in Figure 2f, the SnTe lattice shrinkage with an increasing amount of $NaSbSe_2$ follows Vegard's law in the whole range tested except for x=0.20 (Figure 2f) [41]. The x=0.20 sample surprisingly deviates from the linear trend of the lattice parameters in Figure 2f, which indicates that the solubility limit of $NaSbSe_2$ in SnTe has been reached. This result is consistent with observing minor secondary phases for this high $NaSbSe_2$ concentration.

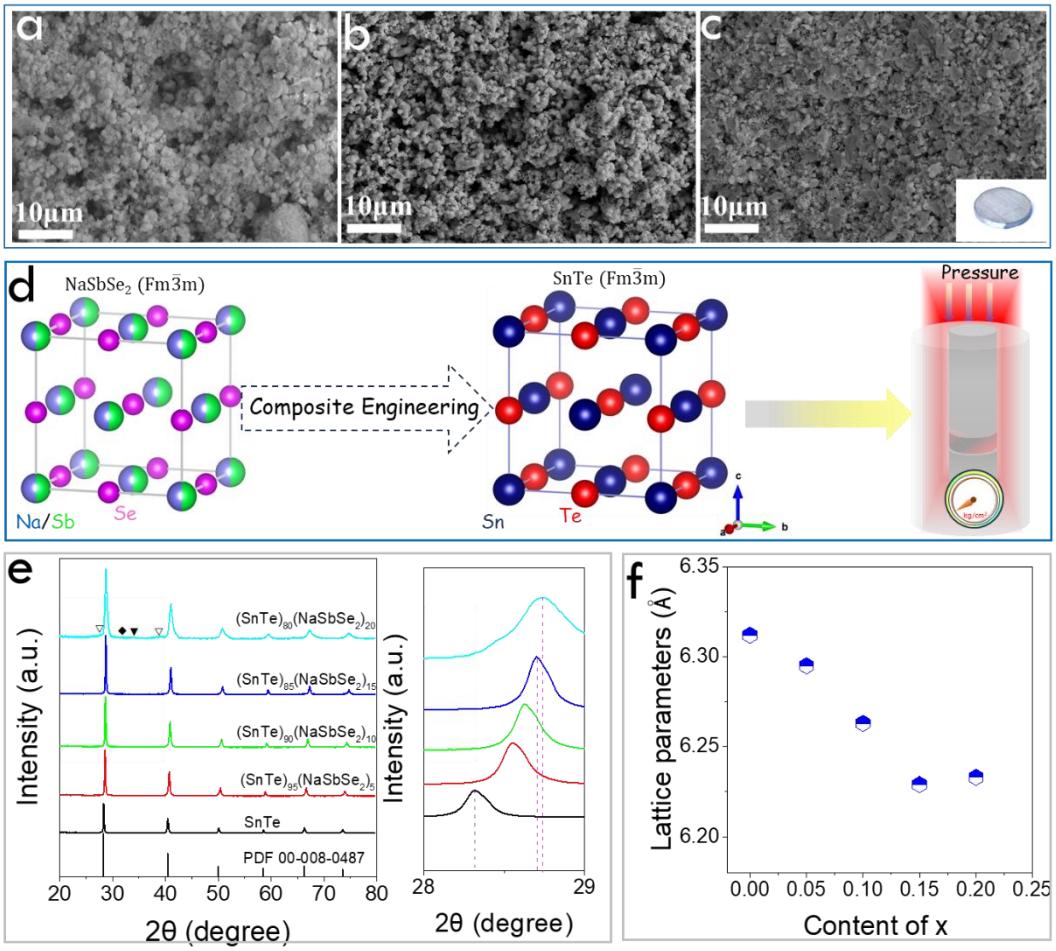


**Figure 2.** (a-c) SEM image of the (a) dried mixture, (b) annealed mixing powders, and (c) fractured pellet surface of $(SnTe)_{0.85}(NaSbSe_2)_{0.15}$. The inset is the corresponding pellet with a diameter of 10 mm. (d) Schematic rock-salt crystal structures of the cubic SnTe and $NaSbSe_2$. (e) XRD patterns for sintered $(SnTe)_{1-x}(NaSbSe_2)_x$ (x=0, 0.05, 0.10, 0.15 and 0.20) pellets and enlarged XRD peaks corresponding to (200) at $2\theta$ between 28°-29°. (f) Calculated lattice parameters for $(SnTe)_{1-x}(NaSbSe_2)_x$ (x=0, 0.05, 0.10, 0.15 and 0.20).

SEM-EDS analysis of the $(SnTe)_{0.85}(NaSbSe_2)_{0.15}$ shows Sn, Te, Na, Sb, and Se to be evenly distributed within the pellet (Figure 3a and b). As shown in the HRTEM image of Figure 3c, some dark contrast areas are assigned to strain clusters caused by severe lattice distortion [42]. Besides, the HRTEM micrograph of Figure 3d identifies an interplanar spacing distance of ~0.321 nm corresponding to the (200) planes of cubic SnTe. The inverse fast Fourier transform (IFFT) image in Figure 3f shows dense dislocations (marked as "⊥"), which can effectively increase phonon scattering. In contrast, the HRTEM analysis of undoped SnTe

shows a defect-free ordered lattice (Figure S8). These results demonstrate that incorporating $NaSbSe_2$ promotes the formation of dislocations in the alloys. In addition, the geometric phase analysis (GPA) verifies the presence of strains in the different directions of $\varepsilon_{xx}$, $\varepsilon_{xy,}$ and $\varepsilon_{yy}$. The obvious strains in the $(SnTe)_{0.85}(NaSbSe_2)_{0.15}$ sample in Figure 3f are caused by substitution point defects and possible vacancies [43]. These strain fields are believed to hamper phonon propagation and reduce lattice thermal conductivity [44].

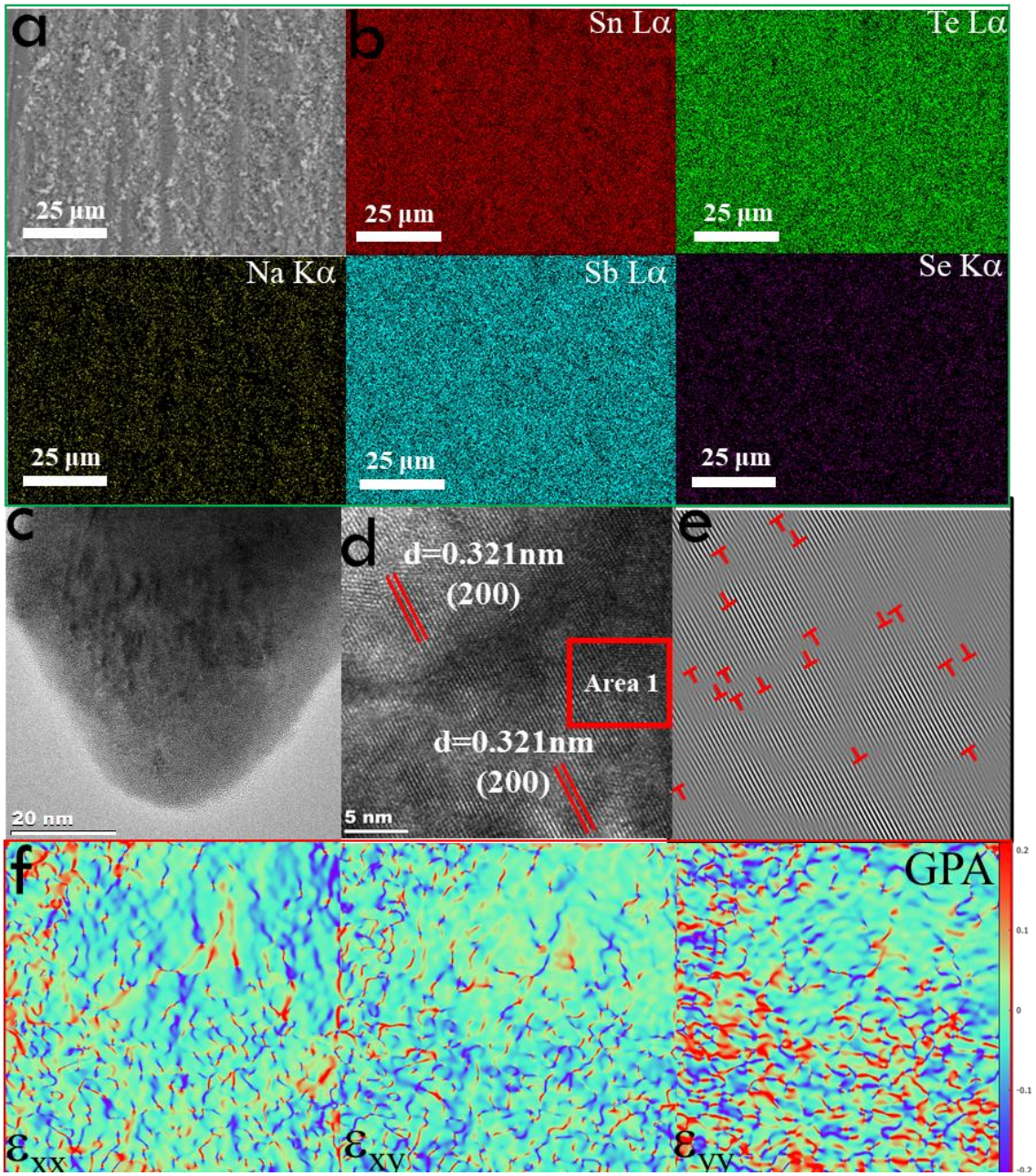


**Figure 3.** (a) SEM image of the polished surface of the sintered $(SnTe)_{0.85}(NaSbSe_2)_{0.15}$ pellet, and (b) the corresponding EDS mappings of Sn, Te, Na, Sb, and Se, respectively. (c,d) HRTEM images. (e) IFFT

image of the selected red region area 1 in (d). (f) GPA results from (d) showing the strain maps of tensors $\varepsilon_{xx}$, $\varepsilon_{xy,}$ and $\varepsilon_{yy}$.

The electronic transport properties of $(SnTe)_{1-x}(NaSbSe_2)_x$ (x=0, 0.05, 0.10, 0.15 and 0.20) samples are plotted in Figure 4a. The electrical conductivity of all these samples decreases monotonically with increasing temperature, exhibiting a degenerate semiconductor behavior. As expected, the electrical conductivity drops significantly with increasing the $NaSbSe_2$ fraction at room temperature. For instance, the undoped SnTe sample without $NaSbSe_2$ has a large electrical conductivity of $3.40\times10^5$ S $m^{-1}$ at room temperature, which decreases from $1.90\times10^5$ S $m^{-1}$ to $1.01\times10^5$ S $m^{-1}$ with increasing $NaSbSe_2$ loadings from 0.05 to 0.20. The room-temperature Hall carrier concentrations $p_H$ is shown in Table S2. The carrier concentration of $(SnTe)_{1-x}(NaSbSe_2)_x$ samples increases with the $NaSbSe_2$ fraction, from $3.20\times10^{20}$ $cm^{-3}$ for un-doped SnTe to $1.23\times10^{21}$ $cm^{-3}$ after $NaSbSe_2$ content of 0.20. In contrast, the charge carrier mobility strongly decreases with the introduction of $NaSbSe_2$, resulting in reduced electrical conductivity. Previous studies have shown that Na doping in the SnTe matrix increases Sn vacancies and, thus, the carrier concentration [11]. Here, we observed that introducing Na and Sb into Sn sites reduces the formation energy of Sn vacancies, thereby ultimately increasing the hole carrier concentration of the alloys [22]. Similar enhancement of carrier concentrations and decreased mobilities are found in the SnTe-based TE studies such as $LiSbTe_2$ [45], $NaSbTe_2$ [8], $CuSbSe_2$ [27], $AgSbSe_2$ [20, 46] and $AgSbTe_2$ [21, 22, 47].

Figure 4b shows the temperature dependence of the Seebeck coefficient for $(SnTe)_{1-x}(NaSbSe_2)_x$ (x=0, 0.05, 0.10, 0.15 and 0.20) pellets. All samples exhibit *p*-type characteristics with positive Seebeck coefficients, indicating that holes dominate the electronic transport. For each $(SnTe)_{1-x}(NaSbSe_2)_x$ sample, the Seebeck coefficient monotonically enhances with temperature. The Seebeck coefficient values at 823 K increase from 131.2 μV $K^{-1}$ for pristine SnTe to 184.3 μV $K^{-1}$ for $(SnTe)_{0.90}(NaSbSe_2)_{0.10}$. However, only for the $(SnTe)_{0.85}(NaSbSe_2)_{0.15}$ sample in the high-temperature region, a significant improvement in the power factor after the introduction of $NaSbSe_2$ is obtained. It is attributed to the significantly reduced electrical conductivity that largely neutralizes the increase of the Seebeck coefficient (Figure 4c). At 823 K, the power factor improves from 1.62 for pure SnTe to 1.77 mW $m^{-1}K^{-2}$ for

$(SnTe)_{0.85}(NaSbSe_2)_{0.15}$. The Seebeck coefficient as a function of carrier concentration at room temperature based on the two-valence band model is shown in Figure 4d. The Seebeck coefficient values of the alloys at room temperature are higher than the theoretical Pisarenko curve (solid black line), which is associated with the reached band convergence [13, 26, 48].

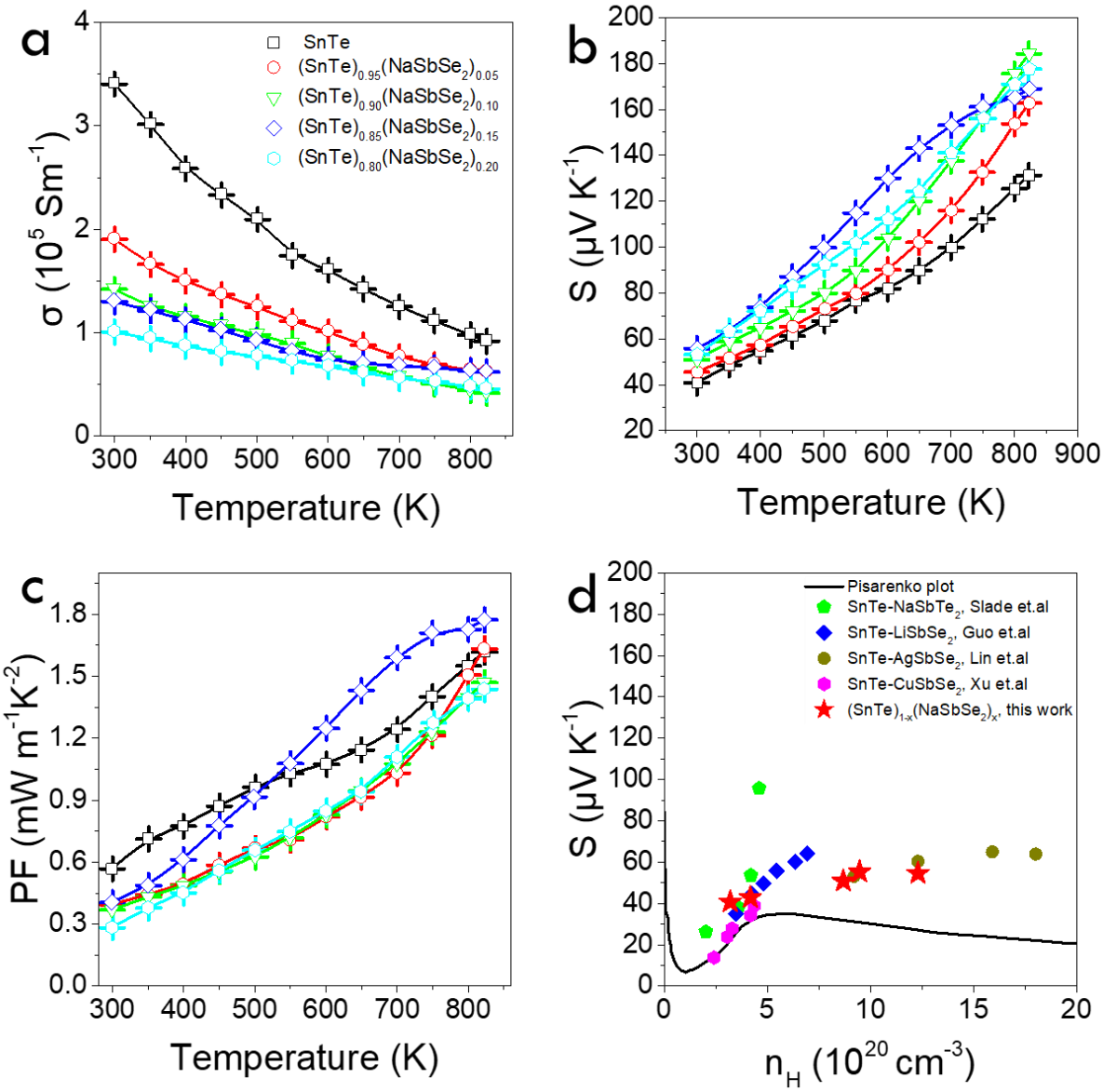


**Figure 4**. Temperature dependence of (a) electrical conductivity, (b) Seebeck coefficient, and (c) power factor of $(SnTe)_{1-x}(NaSbSe_2)_x$ (x=0, 0.05, 0.10, 0.15 and 0.20). (d) Seebeck coefficient as a function of carrier concentration at room temperature. The theoretical Pisarenko curve (solid line) is based on the two valence band model, and comparative data include SnTe-$NaSbTe_2$ [8], SnTe-$LiSbSe_2$ [45], SnTe-$AgSbSe_2$ [20], and SnTe-$CuSbSe_2$ [27] is included.

As shown in Figure 5a, the total thermal conductivity ($\kappa_{tot}$) significantly declines as the

$NaSbSe_2$ fraction increases. The total thermal conductivity drops sharply from 3.36 W $m^{-1}$ $K^{-1}$ for pristine SnTe to 1.50 W $m^{-1}$ $K^{-1}$ for $(SnTe)_{0.95}(NaSbSe_2)_{0.05}$ at 823 K, which further decreases to 1.27 W $m^{-1}$ $K^{-1}$ at x=0.15 and 1.09 W $m^{-1}$ $K^{-1}$ at x=0.20. At ambient temperature, the $\kappa_{tot}$ value of 6.05 W $m^{-1}$ $K^{-1}$ obtained before incorporating $NaSbSe_2$ is decreased to 2.23 W $m^{-1}$ $K^{-1}$ for the $(SnTe)_{0.95}(NaSbSe_2)_{0.05}$ sample, which represents a decline of 171% compared to undoped SnTe. The dramatic reduction of $\kappa_{tot}$ is attributed to the suppression of both electronic and lattice contributions. The electronic thermal conductivity ($\kappa_{ele}$) can be calculated by the Wiedemann-Franz formula $\kappa_{ele} = L\sigma T$, where L, σ, and T are the Lorentz number, electrical conductivity, and absolute temperature, respectively. The Lorentz number L is obtained from a single parabolic band (SPB) model, thus calculated according to the equation $L = 1.5 + \exp\left[-\frac{|S|}{116}\right] \times 10^{-8}$ $V^2K^{-2}$ [49]. The resultant temperature dependence Lorenz number is shown in Figure S9. The calculated $\kappa_{ele}$ is plotted in Figure 5b. In addition, the contribution of lattice thermal conductivity ($\kappa_{lat}$) to the total thermal conductivity is calculated through $\kappa_{lat} = \kappa_{tot} - \kappa_{ele}$. The incorporation of $NaSbSe_2$ significantly decreased the lattice thermal conductivity (Figure 5c), down to a minimum of 0.38 W $m^{-1}$ $K^{-1}$ for $(SnTe)_{0.85}(NaSbSe_2)_{0.15}$ at 823 K, which is even lower than the Debye−Cahill amorphous limit ($\kappa_{lat,\ min}$ = 0.4 W $m^{-1}$ $K^{-1}$) at high temperature for SnTe (Figure 5c) [50]. Figure 5d compares the thermal conductivity of previously reported SnTe-I−V−$VI_2$-alloys [8, 20, 23, 27, 41, 45].

The lattice thermal conductivity is a relatively independent parameter, which can be reduced to a minimum through microstructural defects engineering [51]. To further clarify the origin of the decreased lattice thermal conductivity in $(SnTe)_{1-x}(NaSbSe_2)_x$ samples, the lattice thermal conductivity can be described as follows [52]:

$$\kappa_{lat} = \frac{1}{3} C_V v_g l = \frac{1}{3} C_V v_g^2 \tau \qquad (l = v_g \tau)$$

where $C_V$, $v_g$, $l$, and $\tau$ denote total heat capacity at constant volume, phonon group velocity, phonon mean free path (MFP), and phonon relaxation time, respectively. Achieving lower values of $\kappa_{lat}$ requires low $C_V$, slow $v_g$, and short τ. The usual strategy to minimize τ for reducing $\kappa_{lat}$ is mainly to introduce multi-scale phonon scattering centers. Common phonon scattering centers include point defects (substitutions, interstitials, and vacancies), dislocations and strains, nanostructure precipitates, and grain boundaries [53]. Phonons are scattered at

different rates depending on their frequency on these different defects. For instance, high-frequency phonons (characterized by short wavelengths) can be effectively scattered by point defects, dislocations, and strains can effectively scatter mid-frequency phonons, and long-wavelength phonons can be scattered by grain boundaries and interphases [54]. The total phonon scattering relaxation $\tau_{tot}$

$$\tau^{-1} = \tau_{PD}^{-1} + \tau_{NP}^{-1} + \tau_{PP}^{-1} + \tau_{IF}^{-1} + \tau_{DC}^{-1} \cdots$$

where $\tau_{PD}$, $\tau_{NP}$, $\tau_{PP}$, $\tau_{IF}$, and $\tau_{DC}$ are the relaxation time caused by the point defects, nanoprecipitates, phonon−phonon interactions, interfaces, and dislocation scattering, respectively. In $(SnTe)_{1-x}(NaSbSe_2)_x$ (x=0.05, 0.10, 0.15, and 0.20) samples, the disordered cationic positions should be randomly occupied by Sn, Na, and Sb, while Se atoms replace part of the anionic Te positions. The presence of multiple different atoms in the same position creates more considerable disorder in the system that causes significant phonon scattering [55]. Besides, the presence of strain clusters and dense dislocations was confirmed by the HRTEM images discussed previously. Thus, overall, the incorporation of $NaSbSe_2$ NCs into SnTe introduces various phonon scattering centers such as Sn vacancies, substitution point defects, dislocations, strains, and some impurities in case of x=0.20, which enable a dramatic reduction in $\kappa_{lat}$ through scattering phonons in a wide wavelength range, which, in general, contributes to improving the ZT value [53].

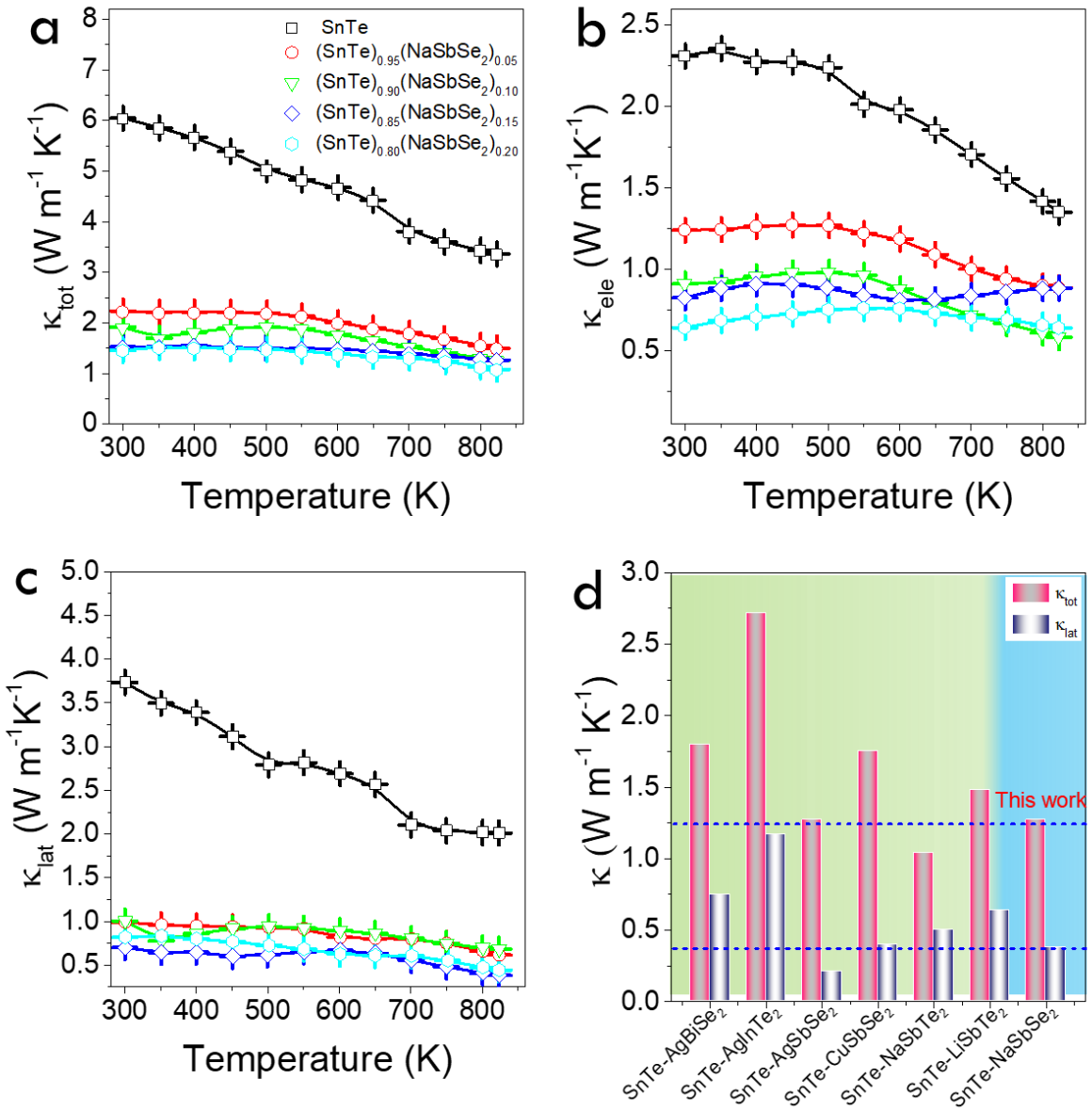


**Figure 5**. Temperature dependence of (a) total thermal conductivity, (b) electrical thermal conductivity, and (c) lattice thermal conductivity of $(SnTe)_{1-x}(NaSbSe_2)_x$ (x=0, 0.05, 0.10, 0.15 and 0.20). (d) Comparison of the total thermal conductivity and lattice thermal conductivity of SnTe-based TE materials: SnTe-$AgBiSe_2$ [23], SnTe-$AgInTe_2$ [41], SnTe-$AgSbSe_2$ [20], SnTe-$CuSbSe_2$ [27], SnTe-$NaSbTe_2$ [8], SnTe-$LiSbTe_2$ [45].

The temperature-dependent TE ZT values of $(SnTe)_{1-x}(NaSbSe_2)_x$ (x=0, 0.05, 0.10, 0.15, and 0.20) samples are plotted in Figure 6a. All the $(SnTe)_{1-x}(NaSbSe_2)_x$ samples display higher ZT values than pristine SnTe due to the band convergence and especially the enhanced phonon scattering brought by the $NaSbSe_2$ incorporation. $(SnTe)_{0.85}(NaSbSe_2)_{0.15}$ reached a peak ZT

value of 1.15 at 823 K, which is ~193% higher than intrinsic SnTe. Besides, the obtained ZT values reported here overcome those of most state-of-the-art SnTe-(I−V−$VI_2$) materials, as summarized in Figure 6b. Additionally, the TE performance of the $(SnTe)_{0.85}(NaSbSe_2)_{0.15}$ sample is stable over the entire measurement temperature range due to its good thermal stability (Figure S10). The above results demonstrate the feasibility of boosting the TE performance of SnTe by synergistically enhancing phonon scattering and band convergence.

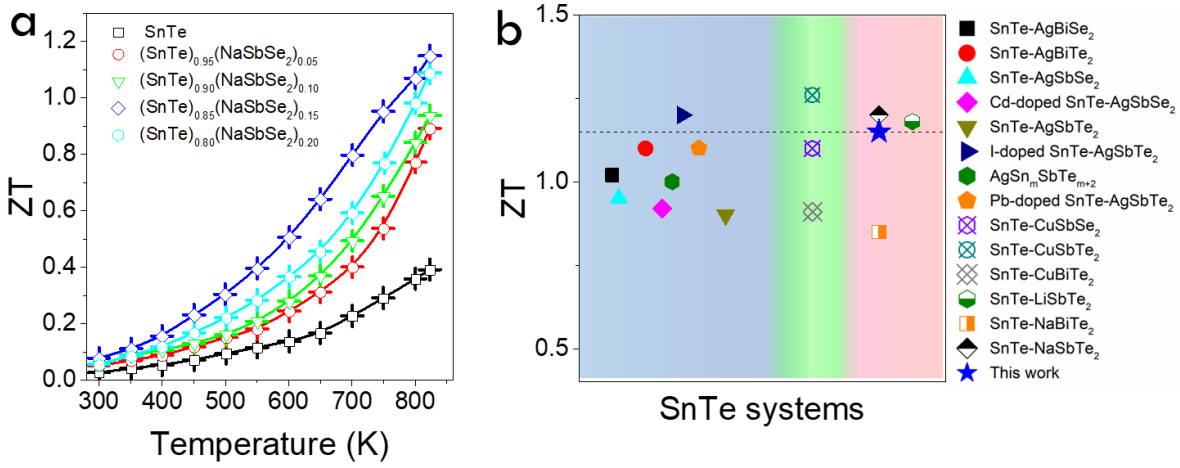


**Figure 6.** Temperature dependence of (a) ZT value of $(SnTe)_{1-x}(NaSbSe_2)_x$ alloys (x=0, 0.05, 0.10, 0.15, and 0.20). (b) Comparison of maximum ZT values of the $(SnTe)_{0.85}(NaSbSe_2)_{0.15}$ and previously reported SnTe-based systems ($AgBiSe_2$ [23], $AgBiTe_2$ [56], $AgSbSe_2$ [20], Cd-$AgSbSe_2$ [46], $AgSbTe_2$/I-doped $AgSbTe_2$ [22], $AgSn_mSbTe_{m+2}$ [57], Pb-doped $AgSbTe_2$ [21], $CuSbSe_2$ [27], $CuSbTe_2$/$CuBiTe_2$ [58], $LiSbTe_2$ [45], $NaSbTe_2$/$NaBiTe_2$ [8]).

## 3. Conclusions

In summary, a series of $(SnTe)_{1-x}(NaSbSe_2)_x$ alloys (x=0, 0.05, 0.10, 0.15, and 0.20) was prepared via the solution mixing, annealing, and hot-pressing of SnTe NPs and $NaSbSe_2$ NCs. Experimental results indicate that $NaSbSe_2$ NCs alloyed with SnTe NPs can significantly increase the Seebeck coefficient of SnTe due to band convergence. Besides, the incorporation of $NaSbSe_2$ substantially reduces the thermal conductivity of SnTe. This phenomenon is explained by considering the addition of $NaSbSe_2$ NCs leading to the occurrence of multiscale defects, such as Sn vacancies, substitutions, dislocations, strain, and even secondary phases. Overall, an ultralow lattice thermal conductivity value of 0.38 W $m^{-1}K^{-1}$ at 823 K was obtained

for the $(SnTe)_{0.85}(NaSbSe_2)_{0.15}$ sample. Ultimately, ZT values up to 1.15 at 823 K were achieved for the $(SnTe)_{0.85}(NaSbSe_2)_{0.15}$ sample, which also showed high thermal stability.

## Declaration of Competing Interest

The authors declare no competing financial interest.

## CRediT authorship contribution statement

Bingfei Nan designed and carried out experiments and wrote a first version of the manuscript. Cheng Chang, Nilotpal Kapuria, Xu Han, Mengyao Li, Kevin M. Ryan, Jordi Arbiol performed characterization of materials and analyzed the obtained data. Andreu Cabot revise the final version of the manuscript.

## Data Availability

Data will be made available on request.

## Acknowledgments

B.F.N. thanks the China Scholarship Council (CSC) for the scholarship support and acknowledges funding from the FWF "Lise Meitner Fellowship" grant agreement M 2889-N. N.K. acknowledges funding from Irish Research Council (IRC) under Grant Number IRCLA/2017/285. K.M.R. acknowledges Science Foundation Ireland (SFI) under the Principal Investigator Program under contract no. 16/IA/4629 and under grant no. SFI 16/M-ERA/3419. ICN2 acknowledges funding from Generalitat de Catalunya 2021SGR00457. This study is part of the Advanced Materials programme and was supported by MCIN with funding from European Union NextGenerationEU (PRTR-C17.I1) and by Generalitat de Catalunya. ICN2 is supported by the Severo Ochoa program from Spanish MCIN / AEI (Grant No.: CEX2021-001214-S) and is funded by the CERCA Programme / Generalitat de Catalunya. ICN2 is founding member of e-DREAM.X [59].

## Appendix A. Supporting information

Supplementary data associated with this article can be found in the online version at XXX.

## References


[1] Z. Bu, X. Zhang, Y. Hu, Z. Chen, S. Lin, W. Li, C. Xiao, Y. Pei, A record thermoelectric efficiency in tellurium-free modules for low-grade waste heat recovery, Nat. Commun. 13(1) (2022) 237.

[2] Z. Liang, C. Xu, S. Song, X. Shi, W. Ren, Z. Ren, Enhanced Thermoelectric Performance of p-Type $Mg_3Sb_2$ for Reliable and Low-Cost all-$Mg_3Sb_2$-Based Thermoelectric Low-Grade Heat Recovery, Adv. Funct. Mater. (2022) 2210016.

[3] B. Qin, L.-D. Zhao, Moving fast makes for better cooling, Science 378(6622) (2022) 832-833.

[4] B. Qin, D. Wang, X. Liu, Y. Qin, J.-F. Dong, J. Luo, J.-W. Li, W. Liu, G. Tan, X. Tang, J.-F. Li, J. He, L.-D. Zhao, Power generation and thermoelectric cooling enabled by momentum and energy multiband alignments, Science 373(6554) (2021) 556-561.

[5] Z. Zhou, Y. Huang, B. Wei, Y. Yang, D. Yu, Y. Zheng, D. He, W. Zhang, M. Zou, J.-L. Lan, J. He, C.-W. Nan, Y.-H. Lin, Compositing effects for high thermoelectric performance of $Cu_2Se$-based materials, Nat. Commun. 14(1) (2023) 2410.

[6] W. Li, S. Lin, X. Zhang, Z. Chen, X. Xu, Y. Pei, Thermoelectric Properties of $Cu_2SnSe_4$ with Intrinsic Vacancy, Chem. Mater. 28(17) (2016) 6227-6232.

[7] Y. Wu, P. Nan, Z. Chen, Z. Zeng, R. Liu, H. Dong, L. Xie, Y. Xiao, Z. Chen, H. Gu, W. Li, Y. Chen, B. Ge, Y. Pei, Thermoelectric Enhancements in PbTe Alloys Due to Dislocation-Induced Strains and Converged Bands, Adv. Sci. 7(12) (2020) 1902628.

[8] T.J. Slade, K. Pal, J.A. Grovogui, T.P. Bailey, J. Male, J.F. Khoury, X. Zhou, D.Y. Chung, G.J. Snyder, C. Uher, V.P. Dravid, C. Wolverton, M.G. Kanatzidis, Contrasting SnTe–$NaSbTe_2$ and SnTe–$NaBiTe_2$ Thermoelectric Alloys: High Performance Facilitated by Increased Cation Vacancies and Lattice Softening, J. Am. Chem. Soc. 142(28) (2020) 12524-12535.

[9] Z. Chen, X. Guo, F. Zhang, Q. Shi, M. Tang, R. Ang, Routes for advancing SnTe thermoelectrics, J. Mater. Chem. A 8(33) (2020) 16790-16813.

[10] M.H. Lee, D.-G. Byeon, J.-S. Rhyee, B. Ryu, Defect chemistry and enhancement of thermoelectric performance in Ag-doped $Sn_{1+\delta-x}Ag_xTe$, J. Mater. Chem. A 5(5) (2017) 2235-2242.

[11] A. Abbas, M. Nisar, Z.H. Zheng, F. Li, B. Jabar, G. Liang, P. Fan, Y.-X. Chen, Achieving High Thermoelectric Performance of Eco-Friendly SnTe-Based Materials by Selective Alloying and Defect Modulation, ACS Appl. Mater. Interfaces 14 (2022) 25802-25811.

[12] D.K. Bhat, U.S. Shenoy, Zn: a versatile resonant dopant for SnTe thermoelectrics, Mater. Today Phys. 11 (2019) 100158.

[13] Q. Zhang, B. Liao, Y. Lan, K. Lukas, W. Liu, K. Esfarjani, C. Opeil, D. Broido, G. Chen, Z. Ren, High thermoelectric performance by resonant dopant indium in nanostructured SnTe, Proc. Natl. Acad. Sci. U.S.A. 110(33) (2013) 13261-13266.

[14] A. Banik, B. Vishal, S. Perumal, R. Datta, K. Biswas, The origin of low thermal conductivity in $Sn_{1-x}Sb_xTe$: phonon scattering via layered intergrowth nanostructures, Energy Environ. Sci. 9(6) (2016) 2011-2019.

[15] Z. Zhou, J. Yang, Q. Jiang, Y. Luo, D. Zhang, Y. Ren, X. He, J. Xin, Multiple effects of Bi doping in enhancing

the thermoelectric properties of SnTe, J. Mater. Chem. A 4(34) (2016) 13171-13175.
[16] A. Banik, U.S. Shenoy, S. Anand, U.V. Waghmare, K. Biswas, Mg Alloying in SnTe Facilitates Valence Band Convergence and Optimizes Thermoelectric Properties, Chem. Mater. 27(2) (2015) 581-587.
[17] R. Al Rahal Al Orabi, J. Hwang, C.-C. Lin, R. Gautier, B. Fontaine, W. Kim, J.-S. Rhyee, D. Wee, M. Fornari, Ultralow Lattice Thermal Conductivity and Enhanced Thermoelectric Performance in SnTe:Ga Materials, Chem. Mater. 29(2) (2017) 612-620.
[18] U.S. Shenoy, D.K. Bhat, Vanadium: A Protean Dopant in SnTe for Augmenting Its Thermoelectric Performance, ACS Sustainable Chem. Eng. 9(38) (2021) 13033-13038.
[19] X. Shi, Z. Ren, When IV−VI Meets I−V−$VI_2$: A Reinvigorating Thermoelectric Strategy for Tin Monochalcogenides, ChemNanoMat 9(1) (2023) e202200396.
[20] S.-X. Lin, X. Tan, H. Shao, J. Xu, Q. Wu, G.-Q. Liu, W.-H. Zhang, J. Jiang, Ultralow Lattice Thermal Conductivity in SnTe by Manipulating the Electron–Phonon Coupling, J. Phys. Chem. C 123(26) (2019) 15996-16002.
[21] T. Hong, D. Wang, B. Qin, X. Zhang, Y. Chen, X. Gao, L.-D. Zhao, Band convergence and nanostructure modulations lead to high thermoelectric performance in $SnPb_{0.04}Te$-y% $AgSbTe_2$, Mater. Today Phys. 21 (2021) 100505.
[22] G. Tan, S. Hao, R.C. Hanus, X. Zhang, S. Anand, T.P. Bailey, A.J.E. Rettie, X. Su, C. Uher, V.P. Dravid, G.J. Snyder, C. Wolverton, M.G. Kanatzidis, High Thermoelectric Performance in SnTe–$AgSbTe_2$ Alloys from Lattice Softening, Giant Phonon–Vacancy Scattering, and Valence Band Convergence, ACS Energy Lett. 3(3) (2018) 705-712.
[23] Q. Zhang, Z. Guo, X. Tan, L. Mao, Y. Yin, Y. Xiao, H. Hu, C. Tan, Q. Wu, G.-Q. Liu, J. Xu, J. Jiang, Effects of $AgBiSe_2$ on thermoelectric properties of SnTe, Chem. Eng. J. 390 (2020) 124585.
[24] Z. Guo, G. Wu, X. Tan, R. Wang, Z. Yan, Q. Zhang, K. Song, P. Sun, H. Hu, C. Cui, G.-Q. Liu, J. Jiang, Synergistic Manipulation of Interdependent Thermoelectric Parameters in SnTe–$AgBiTe_2$ Alloys by Mn Doping, ACS Appl. Mater. Interfaces 14(25) (2022) 29032–29038.
[25] J. Yang, J. Cai, R. Wang, Z. Guo, X. Tan, G. Liu, Z. Ge, J. Jiang, Entropy Engineering Realized Ultralow Thermal Conductivity and High Seebeck Coefficient in Lead-Free SnTe, ACS Appl. Energy Mater. 4(11) (2021) 12738-12744.
[26] M. Zhang, X. Tang, N. Li, G. Wang, G. Wang, A. Liu, X. Lu, X. Zhou, Synergistically promoted thermoelectric performance of SnTe by alloying with $NaBiTe_2$, Appl. Phys. Lett. 116(17) (2020) 173902.
[27] H. Xu, H. Wan, R. Xu, Z. Hu, X. Liang, Z. Li, J. Song, Enhancing the thermoelectric performance of SnTe-$CuSbSe_2$ with an ultra-low lattice thermal conductivity, J. Mater. Chem. A 11 (2023) 4310–4318.
[28] M.D. Nielsen, V. Ozolins, J.P. Heremans, Lone pair electrons minimize lattice thermal conductivity, Energy Environ. Sci. 6(2) (2013) 570-578.
[29] C.-M. Dai, P. Xu, M. Huang, Z.-H. Cai, D. Han, Y. Wu, S. Chen, $NaSbSe_2$ as a promising light-absorber semiconductor in solar cells: First-principles insights, APL Mater. 7(8) (2019) 081122.
[30] A. Putatunda, G. Xing, J. Sun, Y. Li, D.J. Singh, Thermoelectric properties of layered $NaSbSe_2$, J. Phys. Condes. Mat. 30(22) (2018) 225501.
[31] B. Nan, X. Song, C. Chang, K. Xiao, Y. Zhang, L. Yang, S. Horta, J. Li, K.H. Lim, M. Ibáñez, A. Cabot, Bottom-Up Synthesis of SnTe-Based Thermoelectric Composites, ACS Appl. Mater. Interfaces 15(19) (2023) 23380-23389.
[32] Y. Liu, M. Li, S. Wan, K.H. Lim, Y. Zhang, M. Li, J. Li, M. Ibáñez, M. Hong, A. Cabot, Surface Chemistry and Band Engineering in $AgSbSe_2$: Toward High Thermoelectric Performance, ACS Nano 17(12) (2023) 11923-11934.

[33] C. Xing, Y. Zhang, K. Xiao, X. Han, Y. Liu, B. Nan, M.G. Ramon, K.H. Lim, J. Li, J. Arbiol, B. Poudel, A. Nozariasbmarz, W. Li, M. Ibáñez, A. Cabot, Thermoelectric Performance of Surface-Engineered $Cu_{1.5-x}Te$–$Cu_2Se$ Nanocomposites, ACS Nano 17(9) (2023) 8442–8452.

[34] N. Kapuria, B. Nan, T.E. Adegoke, U. Bangert, A. Cabot, S. Singh, K.M. Ryan, Colloidal Synthesis of Multinary Alkali-Metal Chalcogenides Containing Bi and Sb: An Emerging Class of I–V–$VI_2$ Nanocrystals with Tunable Composition and Interesting Properties, Chem. Mater. 35(12) (2023) 4810–4820.

[35] Y. Zhang, C. Xing, Y. Liu, M. Li, K. Xiao, P. Guardia, S. Lee, X. Han, A. Ostovari Moghaddam, J. Josep Roa, J. Arbiol, M. Ibáñez, K. Pan, M. Prato, Y. Xie, A. Cabot, Influence of copper telluride nanodomains on the transport properties of n-type bismuth telluride, Chem. Eng. J. 418 (2021) 129374.

[36] Y. Zhang, Y. Liu, M. Calcabrini, C. Xing, X. Han, J. Arbiol, D. Cadavid, M. Ibañez, A. Cabot, Bismuth telluride-copper telluride nanocomposites from heterostructured building blocks, J. Mater. Chem. C 8 (2020) 14092-14099.

[37] M. Ibáñez, Z. Luo, A. Genç, L. Piveteau, S. Ortega, D. Cadavid, O. Dobrozhan, Y. Liu, M. Nachtegaal, M. Zebarjadi, J. Arbiol, M.V. Kovalenko, A. Cabot, High-performance thermoelectric nanocomposites from nanocrystal building blocks, Nat. Commun. 7(1) (2016) 10766.

[38] R. Moshwan, W.-D. Liu, X.-L. Shi, Q. Sun, H. Gao, Y.-P. Wang, J. Zou, Z.-G. Chen, Outstanding thermoelectric properties of solvothermal-synthesized $Sn_{1-3x}In_xAg_{2x}Te$ micro-crystals through defect engineering and band tuning, J. Mater. Chem. A 8(7) (2020) 3978-3987.

[39] S. Duan, W. Xue, H. Yao, X. Wang, C. Wang, S. Li, Z. Zhang, L. Yin, X. Bao, L. Huang, X. Wang, C. Chen, J. Sui, Y. Chen, J. Mao, F. Cao, Y. Wang, Q. Zhang, Achieving High Thermoelectric Performance by $NaSbTe_2$ Alloying in GeTe for Simultaneous Suppression of Ge Vacancies and Band Tailoring, Adv. Energy Mater. 12(3) (2022) 2103385.

[40] L. Wang, S. Chang, S. Zheng, T. Fang, W. Cui, P.-p. Bai, L. Yue, Z.-G. Chen, Thermoelectric Performance of Se/Cd Codoped SnTe via Microwave Solvothermal Method, ACS Appl. Mater. Interfaces 9(27) (2017) 22612-22619.

[41] A. Banik, U.S. Shenoy, S. Saha, U.V. Waghmare, K. Biswas, High Power Factor and Enhanced Thermoelectric Performance of SnTe-$AgInTe_2$: Synergistic Effect of Resonance Level and Valence Band Convergence, J. Am. Chem. Soc. 138(39) (2016) 13068-13075.

[42] P. Peng, C. Wang, S. Cui, C. Wang, J. Chen, M. Hao, X. Huang, X. Wang, Y. Wang, Z. Cheng, J. Wang, Achieving Ultralow Lattice Thermal Conductivity and High Thermoelectric Performance in SnTe by Alloying with $MnSb_2Se_4$, ACS Appl. Mater. Interfaces 15(38) (2023) 45016–45025.

[43] L. Fu, K. Jin, D. Zhang, C. Zhang, H. Nie, Z. Zhen, P. Xiong, M. Huang, J. He, B. Xu, Rashba effect and point-defect engineering synergistically improve thermoelectric performance of the entropy-stabilized $Sn_{0.8}Ge_{0.2}Te_{0.8}Se_{0.2}$ alloy, J. Mater. Chem. A (2023).

[44] J. Dong, Y. Jiang, Y. Sun, J. Liu, J. Pei, W. Li, X.Y. Tan, L. Hu, N. Jia, B. Xu, Q. Li, J.-F. Li, Q. Yan, M.G. Kanatzidis, Discordant Distortion in Cubic GeMnTe2 and High Thermoelectric Properties of $GeMnTe_2$-x%SbTe, J. Am. Chem. Soc. 145( 3) (2023) 1988–1996.

[45] F. Guo, J. Zhu, B. Cui, Y. Sun, X. Zhang, W. Cai, J. Sui, Compromise of thermoelectric and mechanical properties in $LiSbTe_2$ and $LiBiTe_2$ alloyed SnTe, Acta Mater. 231 (2022) 117922.

[46] J. He, J. Xu, X. Tan, G.-Q. Liu, H. Shao, Z. Liu, H. Jiang, J. Jiang, Synthesis of SnTe/$AgSbSe_2$ nanocomposite as a promising lead-free thermoelectric material, J. Materiomics 2(2) (2016) 165-171.

[47] Y. Liu, X. Zhang, P. Nan, B. Zou, Q. Zhang, Y. Hou, S. Li, Y. Gong, Q. Liu, B. Ge, O. Cojocaru-Mirédin, Y. Yu, Y. Zhang, G. Chen, M. Wuttig, G. Tang, Improved Solubility in Metavalently Bonded Solid Leads to

Band Alignment, Ultralow Thermal Conductivity, and High Thermoelectric Performance in SnTe, Adv. Funct. Mater. 32(47) (2022) 2209980.
[48] G. Tan, F. Shi, S. Hao, H. Chi, L.-D. Zhao, C. Uher, C. Wolverton, V.P. Dravid, M.G. Kanatzidis, Codoping in SnTe: Enhancement of Thermoelectric Performance through Synergy of Resonance Levels and Band Convergence, J. Am. Chem. Soc. 137(15) (2015) 5100-5112.
[49] H.-S. Kim, Z.M. Gibbs, Y. Tang, H. Wang, G.J. Snyder, Characterization of Lorenz number with Seebeck coefficient measurement, APL Mater. 3(4) (2015) 041506.
[50] D.G. Cahill, S.K. Watson, R.O. Pohl, Lower limit to the thermal conductivity of disordered crystals, Phys. Rev. B 46(10) (1992) 6131-6140.
[51] Z. Guo, Y.-K. Zhu, M. Liu, X. Dong, B. Sun, F. Guo, Q. Zhang, J. Li, W. Gao, Y.-d. Fu, W. Cai, J. Sui, Z. Liu, Cubic phase stabilization and thermoelectric performance optimization in $AgBiSe_2$–SnTe system, Mater. Today Phys. (2023) 101238.
[52] B. Qin, D. Wang, L.-D. Zhao, Slowing down the heat in thermoelectrics, InfoMat 3(7) (2021) 755-789.
[53] Z. Chen, X. Zhang, Y. Pei, Manipulation of Phonon Transport in Thermoelectrics, Adv. Mater. 30(17) (2018) 1705617.
[54] Y. Shtern, A. Sherchenkov, M. Shtern, M. Rogachev, D. Pepelyaev, Challenges and perspective recent trends of enhancing the efficiency of thermoelectric materials on the basis of PbTe, Mater. Today Commun. 37 (2023) 107083.
[55] M. Dutta, K. Pal, M. Etter, U.V. Waghmare, K. Biswas, Emphanisis in Cubic $(SnSe)_{0.5}(AgSbSe_2)_{0.5}$: Dynamical Off-Centering of Anion Leads to Low Thermal Conductivity and High Thermoelectric Performance, J. Am. Chem. Soc. 143(40) (2021) 16839-16848.
[56] G. Tan, F. Shi, H. Sun, L.-D. Zhao, C. Uher, V.P. Dravid, M.G. Kanatzidis, SnTe–$AgBiTe_2$ as an efficient thermoelectric material with low thermal conductivity, J. Mater. Chem. A 2(48) (2014) 20849-20854.
[57] M.-K. Han, J. Androulakis, S.-J. Kim, M.G. Kanatzidis, Lead-Free Thermoelectrics: High Figure of Merit in p-type $AgSn_mSbTe_{m+2}$, Adv. Energy Mater. 2(1) (2012) 157-161.
[58] W. He, N. Li, H. Wang, G. Wang, G. Wang, X. Lu, X. Zhou, Multiple Effects Promoting the Thermoelectric Performance of SnTe by Alloying with $CuSbTe_2$ and $CuBiTe_2$, ACS Appl. Mater. Interfaces 13(44) (2021) 52775–52782.
[59] J. Arbiol, R. Ciancio, R.E. Dunin-Borkowski, R. Holmestad, A.I. Kirkland, M. Kociak, G. Kothleitner, E. Snoeck, J. Verbeeck, e-DREAM: the European Distributed Research Infrastructure for Advanced Electron Microscopy, Microscopy and Microanalysis 28(S1) (2022) 2900-2902.